Low-Cycle Fatigue Characteristics of Sn-Based Solder Joints

K.O. LEE,[1,3] JIN YU,[1] T.S. PARK,[2] and S.B. LEE[2]

1.—Department of Materials Science and Engineering, Korea Advanced Institute of Science and Technology, Daejon, 305-701, South Korea. 2.—Department of Mechanical Engineering, Korea Advanced Institute of Science and Technology. 3.—E-mail: sam813@kaist.ac.kr

Low-cycle, lap-shear fatigue behavior of Sn-based, Pb-free solder alloys, Sn-3.5Ag, Sn-3.5Ag-Cu, Sn-3.5Ag-Bi, and Sn-0.7Cu, were studied at room temperature using specimens with printed circuit board (PCB)/solder/PCB structure under total displacement of ±10 μm, 12 μm, 15 μm, and 20 μm. The fatigue lives of various solder joint materials, defined as 50% load drop, were correlated with the fracture paths and analyzed using the Coffin–Manson relation, Morrow's plastic-energy dissipation model, and Solomon's load-drop parameter. The Sn-3.5Ag, Sn-0.7Cu eutectics, and Sn-3.5Ag-Cu ternary alloys showed the same level of fatigue resistance, while Bi-containing alloys showed substantially worse fatigue properties. Cross-sectional fractography revealed cracks initiated at the solder wedge near the solder mask and subsequently propagated into the solder matrix in the former group of alloys, in contrast with the crack propagation along the solder/under bump metallurgy (UBM) interfaces in the Sn-3.5Ag-Bi alloys. Inferior fatigue resistance of Bi-containing alloys was ascribed to high matrix hardness, high stiffness, possible Bi segregation to the interface, and high residual stress in the interfacial area.

Key words: Low-cycle fatigue, lead-free solder, Coffin–Manson relationship, Morrow energy mode, Solomon parameter

INTRODUCTION

Tin-lead eutectic alloys have been commonly used as solder material in microelectronic components. Environmental concerns on the toxicity of lead have resulted in legislation forbidding the use of lead in microelectronics products in the near future, prompting intensive searches for lead-free solder alloys.

The fatigue failure of a solder joint in electronic packages mainly arises from the thermal mismatch stress of various components with different thermal-expansion coefficients during power cycling. For solder materials, even room temperature is greater than 0.6 T_m (melting temperature), where creep is the dominant deformation mode,[1] and the creep-fatigue interaction is the dominant mode of failure during thermal cycling. In that context, the creep and fatigue properties of lead-free solders have been studied extensively using bulk specimens.[2–7] However, as pointed out by Song et al.,[8] bulk materials usually have quite different microstructures from the actual solder-joint materials and, thereby, different mechanical properties, too. During the solder reflow process, solder joints with small material volume solidify rapidly, resulting in an as-cast microstructure with fine grain size,[9] and often, solder compositions vary because of the dissolution of under bump metallurgy (UBM) materials into the solder.[10] Actual thermal-fatigue failure of solder joints is a quite complex phenomenon that involves creep deformation of the composite microstructure and fatigue crack propagation along various paths: through the solder matrix, along the solder/intermetallic compound (IMC) interface, and through the brittle IMC layers.

In this study, low-cycle fatigue characteristics of Sn-based, lead-free solders were investigated at room temperature using specimens with actual solder joints, and fatigue lives of various solder alloys were compared. Then, fatigue resistance was analyzed using the Coffin–Manson relation, Morrow's plastic-energy dissipation model, and Solomon's parameter.

(Received May 30, 2003; accepted July 29, 2003)

Table I. Chemical Composition of Sn-Based Solder Alloys (Wt.%)

Alloy	Sn	Ag	Bi	Cu
Sn-3.5Ag	95.7	3.61	—	—
Sn-3.5Ag-0.75Cu	95.1	3.65	—	0.75
Sn-3.5Ag-1.5Cu	94.6	3.49	—	1.48
Sn-3.5Ag-2.5Bi	93.7	3.57	2.51	—
Sn-3.5Ag-7.5Bi	88.5	3.63	7.62	—
Sn-0.7Cu	99.4	—	—	0.57

EXPERIMENTAL PROCEDURE

The chemical composition of six Sn-based solder alloys under investigation are presented in Table I, and schematic diagrams showing the lap-shear fatigue fixture and UBM structure are given in Fig. 1a and b, respectively. The solder balls of 0.76-mm diameter and 1.27-mm pitch were mounted to FR-4 printed circuit boards (PCBs), and the UBM structure consists of Cu/Ni/Au surface finishes (35-μm, 1-μm, and 0.05-μm thick, respectively) with a pad-opening diameter of 0.594 mm. A typical temperature profile during the solder reflow process is shown in Fig. 2, and the time above 220°C (eutectic point of Sn-3.5Ag) was 110 sec. After solder reflow, the PCB/solder/PCB structure was mounted to a stainless-steel grip using an epoxy adhesive (cyanoarcylate).

The micromechanical test system used for the fatigue experiment has a servomotor attached to a ball screw-driven rail table to apply load to the specimen, and the displacement between grips was controlled to the accuracy of 50 nm using a computer-controlled feedback system and a linear

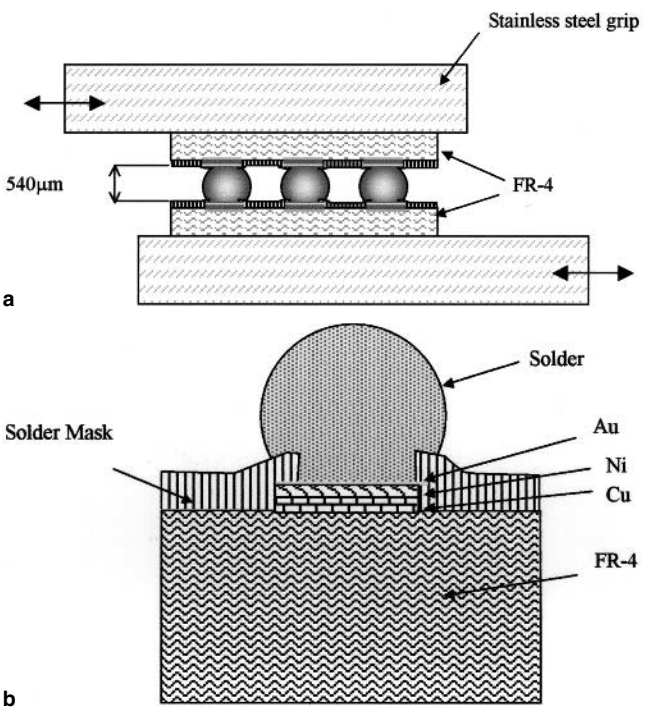

Fig. 1. Schematic diagrams showing (a) the lap-shear fatigue fixtures and (b) UBM structure over the FR-4 substrate.

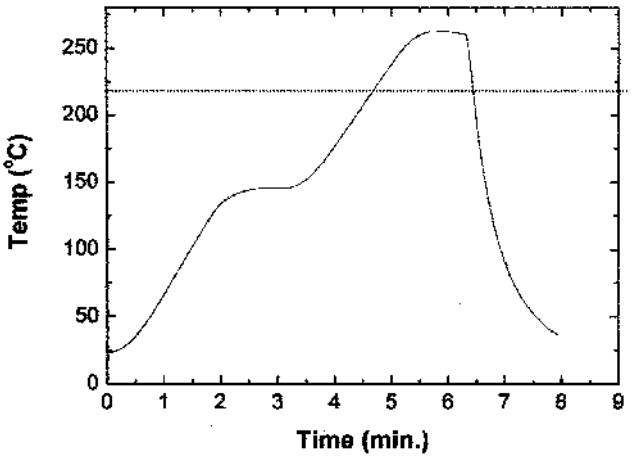

Fig. 2. A typical temperature-time profile in the reflow oven used.

variable-differential transformer.[11] Saw-tooth displacement waves with a frequency of 1/30 Hz were applied at room temperature under total displacement amplitudes of ±10 μm, 12 μm, 15 μm, and 20 μm, with time lags between the displacement and load cycles caused by the time-dependent plasticity.

Typical load-displacement hysteresis under the displacement control tests are given in Fig. 3a. The load amplitude, the difference between the maximum and minimum loads, decreases with the load cycle, presumably, because of the propagation of fatigue cracks. Then, the number of load cycles that gave 50% load drop was defined as the fatigue life, as shown in Fig. 3b. Because the total displacement (Δ_T) is the sum of the solder-ball displacement (Δ_S) and the parasitic displacement (Δ_P) coming from the loading systems (composed of a PCB, adhesives, and stainless-steel grips), Δ_P was measured using specimens without solder-ball attachment between the PCBs, and subsequently subtracted from Δ_T to give Δ_S. Figure 4a demonstrates measured Δ_P under varying Δ_T amplitudes. Note that the parasitic displacement was fully elastic and reproducible. Typical load-displacement (Δ_S) hysteresis of the Sn-3.5Ag-0.75Cu alloy after the Δ_P subtraction for $\Delta_T = \pm 15$ μm are shown in Fig. 4b at various fatigue cycles, and the area inside the hysteresis refers to the plastic work dissipated by the solder material during load cycles.

Fatigue tests were performed after ten days at room temperature after solder reflow, which is known to stabilize the solder microstructure by age softening.[12] After testing, the solders were mounted and mechanically polished with 0.05-μm alumina slurry, etched with a solution containing HNO_3, HCl, and CH_3OH, and were examined using an optical microscope and scanning electron microscope (SEM).

EXPERIMENTAL RESULTS AND DISCUSSION

Optical micrographs of reflowed solders before fatigue are shown in Fig. 5. During reflow, all the Au (about 0.05 wt.%) on the pad is dissolved into the

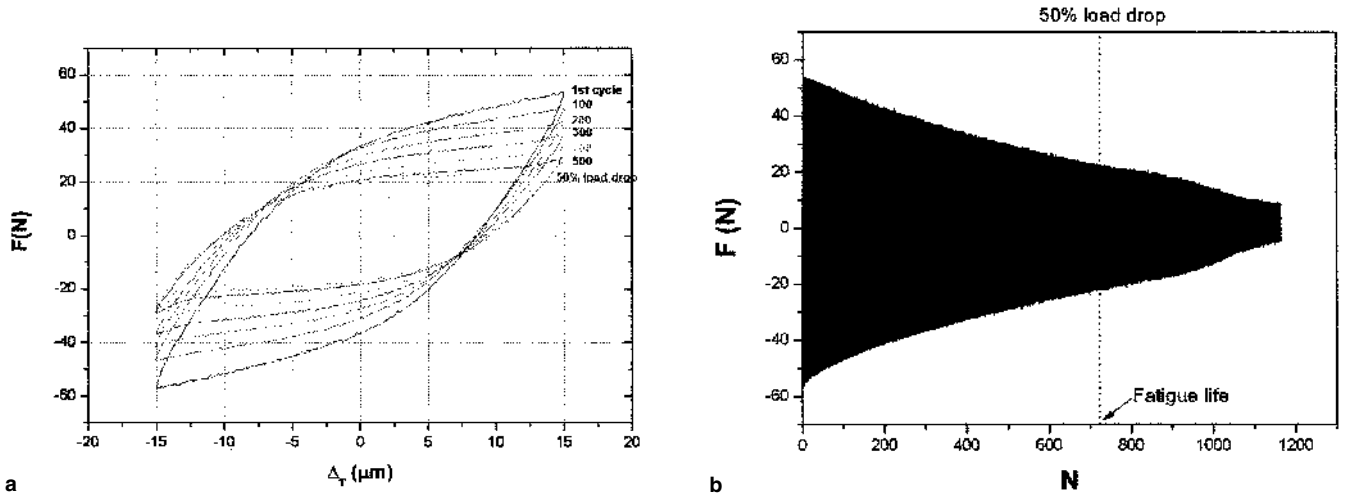

Fig. 3. (a) Force versus displacement hysteresis and (b) the corresponding load drop with fatigue cycles in the Sn-3.5Ag-0.75Cu alloy.

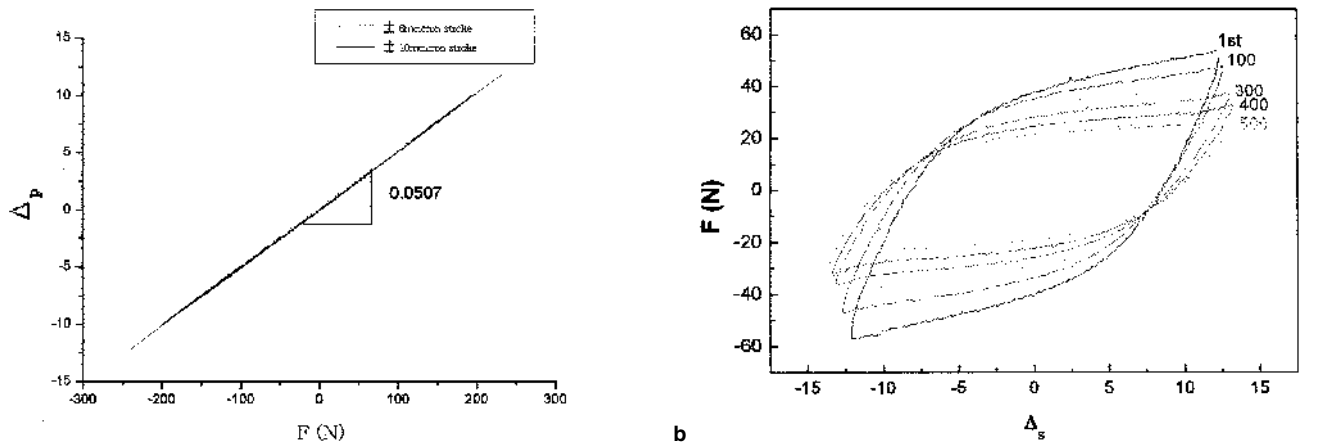

Fig. 4. (a) Parasitic displacement of the loading system and (b) the force versus displacement hysteresis of the Sn-3.5Ag-0.75 solder alloy after the subtraction of Δ_P.

solder matrix, and only Ni_3Sn_4 formed at the solder/UBM interface remains. The white region in the figure is the primary β-Sn dendrites, which were surrounded by a dark eutectic phase that is composed of tiny Ag_3Sn precipitates embedded in the β-Sn phases. Note that the volume of the β-Sn phase was largest for the Sn-0.7Cu alloy. Analyses of the solder matrix by energy dispersive x-ray analysis revealed Cu_6Sn_5 phases in the Sn-3.5Ag-Cu alloys. The Ni_3Sn_4 found at the solder/UBM interface had a layer-type structure that did not show faceted IMC interfaces with the solder, which is consistent with the report by Kang et al.[10] The average IMC thickness was less than 1.5 μm in most cases.

Variations of the maximum force (F_{max}) in the force-displacement hysteresis with the load cycles at several Δ_T strokes are shown in Fig. 6 for the six alloys. Note the following. (1) the magnitude of F_{max} in the beginning of the load cycle decreases in the order of 7.5Bi, 2.5Bi, 1.5Cu, 0.75Cu, SnAg, and SnCu alloys. (2) Bi-containing alloys showed drastic decreases in F_{max} after certain load cycles, implying fast fatigue-crack growth rate (da/dN) during the period. Load drop in all the other alloys were gradual. (3) With increased Δ_T, the load-drop process was accelerated because of higher da/dN, and the trend was strong for the Bi-containing alloys. (4) Relative trends among alloys were more or less unaffected by Δ_T.

The effects of Cu or Bi addition on the fatigue behavior of the Sn-3.5Ag binary alloy are shown in Fig. 7. The fatigue resistance increased slightly with Cu addition up to 0.75%, but tended to decrease with further additions. From Fig. 5, large particles of Cu_6Sn_5 were found only in Sn-3.5Ag-1.5Cu, not in Sn-3.5Ag or Sn-3.5Ag-0.75Cu. From the binary phase diagram, Cu_6Sn_5 precipitates must be in Sn-3.5Ag-0.75Cu,[13] but are too tiny to be observed with the optical microscope. The increase of fatigue resistance from Sn-3.5Ag to Sn-3.5Ag-0.75Cu results from the precipitation and solid-solution hardening with Cu addition. However, the dramatic increase of the Cu_6Sn_5 size from Sn-3.5Ag-0.75Cu to Sn-3.5Ag-1.5Cu had negative effects on fatigue resistance because the interface between Cu_6Sn_5 precipitates and the Sn matrix can act as the crack initiation sites.[9] On the other hand, additions of Bi had deleterious effects on the fatigue life at all Δ values.

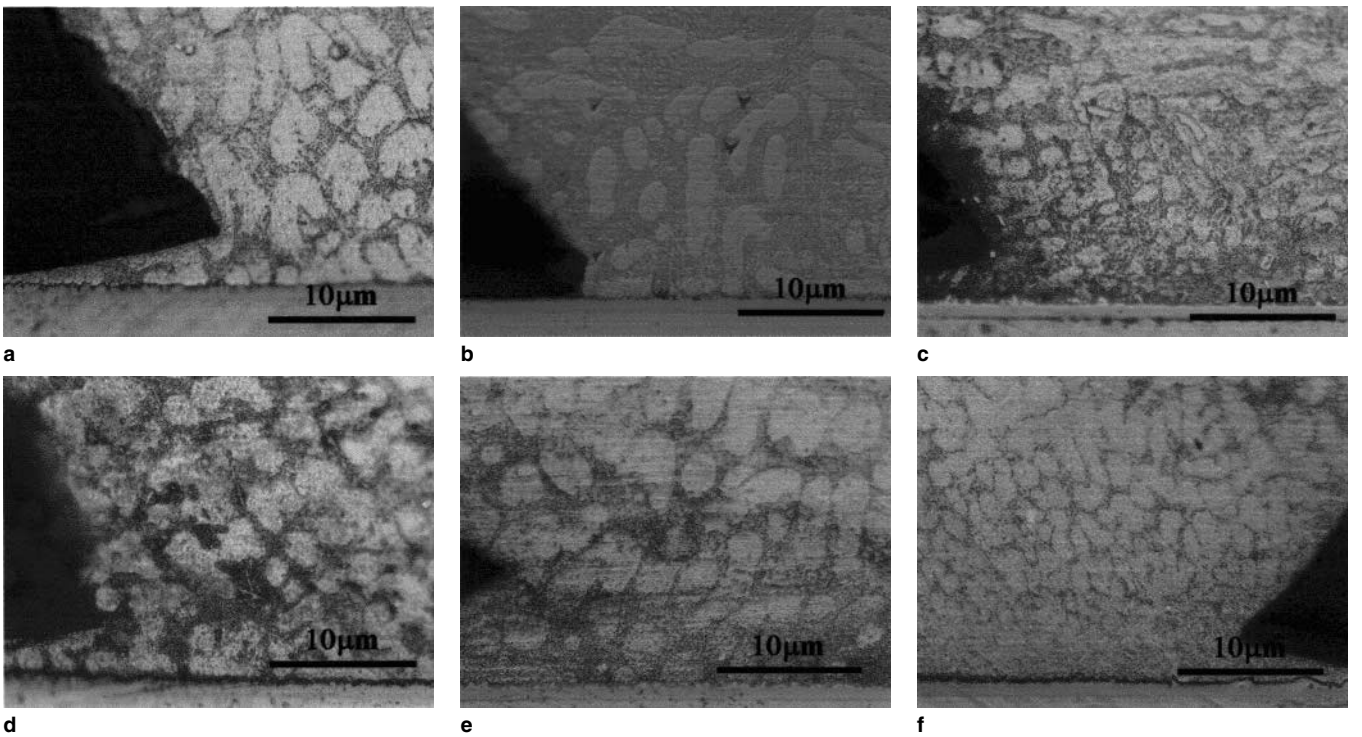

Fig. 5. Optical micrographs of (a) Sn-3.5Ag, (b) Sn-3.5Ag-0.75Cu, (c) Sn-3.5Ag-1.5Cu, (d) Sn-3.5Ag-2.5Bi, (e) Sn-3.5Ag-7.5Bi, and (f) Sn-0.7Cu before the fatigue test.

The fracture surfaces of lead-free solders after fatigue failure are shown in Fig. 8. Fatigue cracks follow the solder/UBM interfaces after a few cycles in the Bi-containing alloys, but cut across the β-Sn/eutectic lamella in the solder for the SnAg, SnAgCu, and SnCu alloys. Detailed observations of the solder/UBM interface areas using a backscattered SEM revealed a couple of salient features regarding the difference of the failure locus, as shown in Fig. 9. The fatigue crack propagated along the Ni_3Sn_4/Ni_3P interface for the Bi-containing alloys, where the thin Ni_3P layers were a byproduct of the reaction-assisted self-crystallization of amorphous Ni(8P) during reflow.[14] It is known that the self-crystallization of Ni(P) and concomitant formation of Ni_3Sn_4 produce high residual stress in the layer.[15] The reason why the fatigue crack followed the interface only in the Bi-containing alloys remains unclear at the moment. It appears that either the presence of high residual stress in the region or Bi segregation to the Ni_3P/Ni_3Sn_4 interface lowered the fracture toughness of the normally tough interface. A parallel work on the fatigue behavior of Sn-3.5Ag-Bi alloys on Cu showed crack propagation mainly on solder/Cu_6Sn_5 interfaces,[16] suggesting that the failure location was affected by the type of UBM.

In the case of Cu-containing alloys, there was no fatigue crack propagation along the Ni_3P/IMC interface, even though some microcracking of the brittle Ni_3Sn_4 IMC was observed during the fatigue cycles. However, these microcracks did not interconnect to become the main crack, and the fatigue failure occurred in the solder matrix. It is not known whether this is the result of lower fracture toughness of the solder matrix than the Ni_3P/IMC interface in the Cu-containing alloys or from the notch that was introduced far above the solder/UBM interface during the photoresist masking process.

The relation between the fatigue life and plastic strain can be described by the Coffin–Manson's relation:

$$\Delta\gamma_p N_f^n = C \quad (1)$$

where $\Delta\gamma_p$ is the plastic strain range, N_f is fatigue life, and n and C are material constants. The plastic strain ($\Delta\gamma_p$) was obtained by subtracting the elastic strain ($\Delta\gamma_e$) from the total strain ($\Delta\gamma_T$), which could be found by extrapolating the initial tangent of the unloading curve of the hysteresis, as shown in Fig. 10. Using the fatigue life defined as the load cycle that gives 50% load drop, a Coffin–Manson type plot was made in Fig. 11, and the material constants n and C of Eq. 1 for various Sn-based solders are summarized in Table II. The Sn-3.5Ag, Sn-0.7Cu eutectics, and Sn-3.5Ag-Cu ternary alloys had the same level of fatigue resistance, while additions of Bi deteriorated the fatigue properties. It appears that Sn-3.5Ag-0.75Cu and Sn-0.7Cu alloys showed slightly better fatigue resistance than Sn-3.5Ag or Sn-3.5Ag-1.5Cu alloys, but with the scatter of data in Fig. 11, it is difficult to be conclusive. The addition of Bi reduced the fatigue life by an order of magnification at all $\Delta\gamma_p$ levels. The Sn-0.7Cu eutectic had a softer matrix and poorer creep resistance than Sn-3.5Ag or Sn-3.5Ag-Cu alloys but had the same fatigue resistance.[9] The

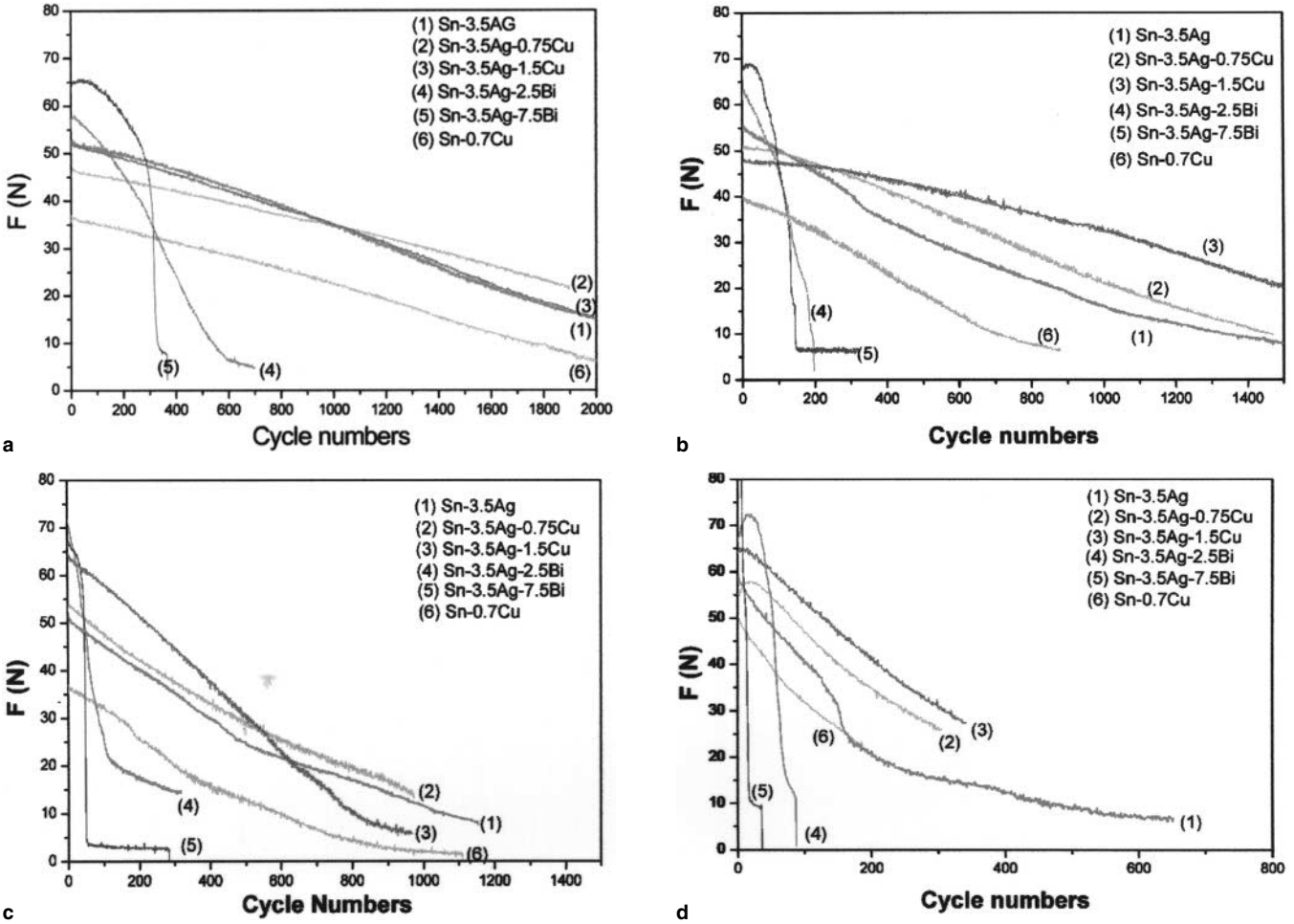

Fig. 6. Variation of maximum force of the hysteresis with the cycle numbers under (a) ±10 μm, (b) ±12 μm, (c) ±15 μm, and (d) ±20 μm stroke for various Sn-based alloys.

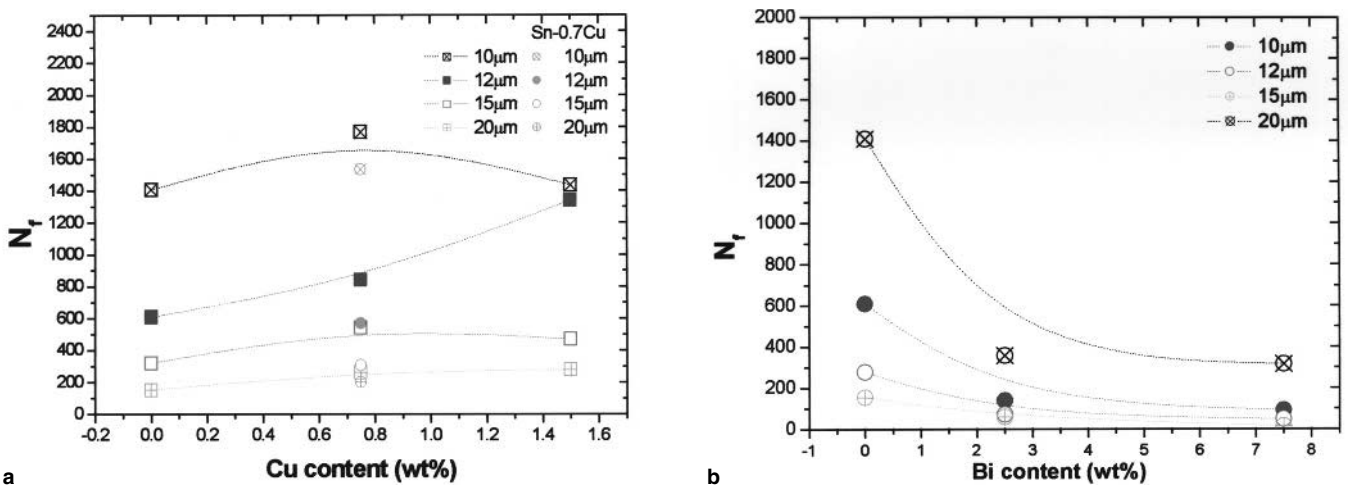

Fig. 7. Effect of (a) Cu and (b) Bi addition on fatigue life of the Sn-3.5Ag alloy under several Δ_T conditions.

fatigue properties of Sn-3.5Ag-Cu alloys noted previously differ slightly from those of bulk specimens. According to Kariya and Otsuka,[2] the fatigue properties of bulk Sn-based, solder specimens decrease with the Cu contents, which is different from what was observed here. The difference may arise from differences in microstructures coming from different solidification rates and composition between the bulk and the joint specimens, which were affected by the surface finish treatment or UBM.

Another method of predicting fatigue life is using the Morrow energy model[17,18] where the plastic-strain energy density (ΔW) is used instead of the plastic strain:

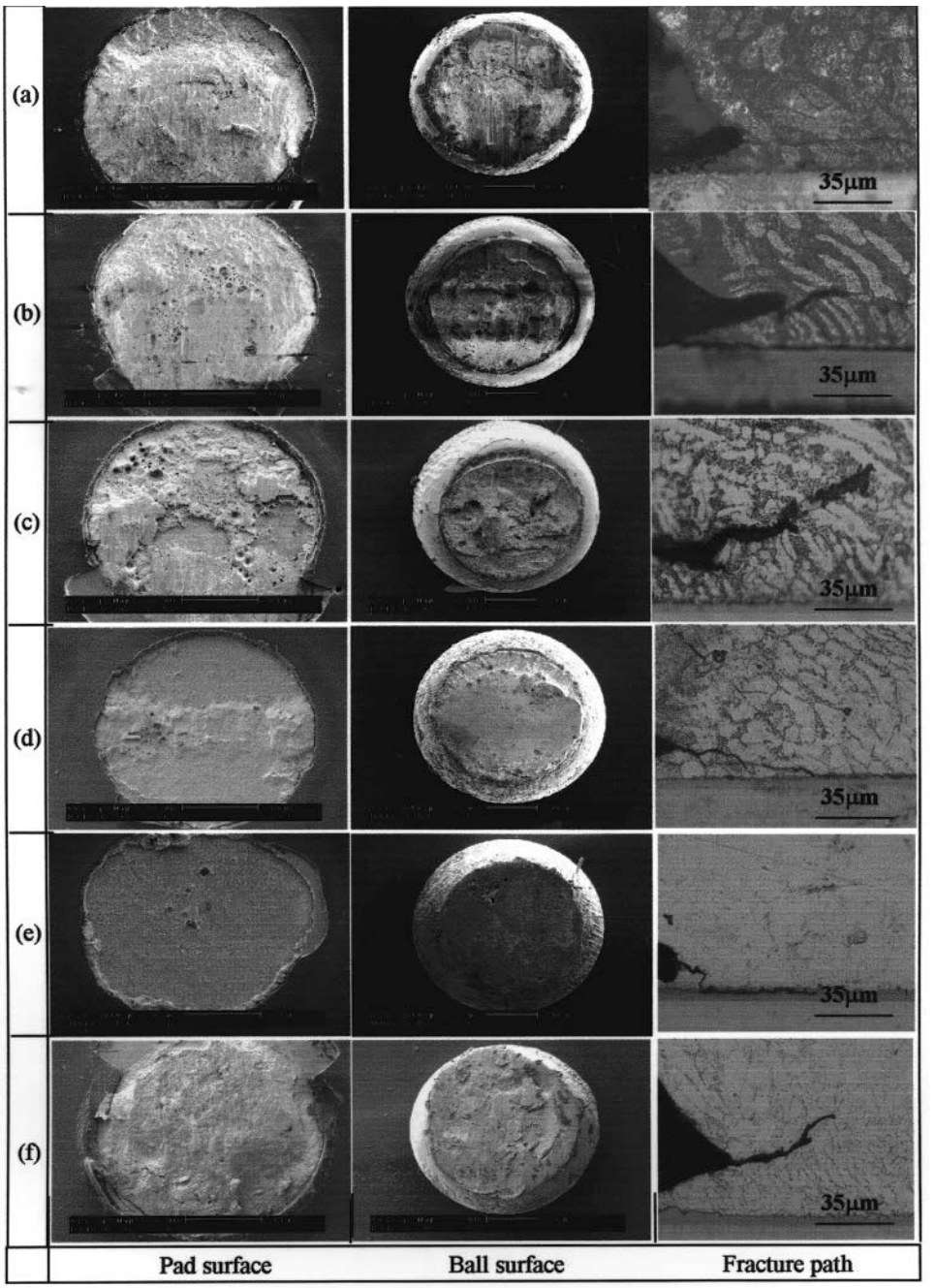

Fig. 8. A macroscopic fracture surface of pad and solder surfaces after fatigue failure and the cross-sectional view of the failure paths of (a) Sn-3.5Ag, (b) Sn-3.5Ag-0.75Cu, (c) Sn-3.5Ag-1.5Cu, (d) Sn-3.5Ag-2.5Bi, (e) Sn-3.5Ag-7.5Bi, and (f) Sn-0.7Cu alloys for $\Delta_T = 15$ μm.

$$N_f^m \Delta W = C \quad (2)$$

Here, m and C are material constants, and the plastic-strain energy density was determined from the area of the first few hysteresis loops. Prediction of the Morrow model is presented in Fig. 12, which is more or less similar to those of the Coffin–Manson equation. A minor difference is that the Morrow model predicts slightly inferior fatigue resistance for the Sn-3.5Ag and Sn-0.7Cu eutectic alloys compared to the Sn-3.5Ag-Cu alloys, particularly at large Δ_T.

In Fig. 6, we observed that the load dropped after few fatigue cycles by the reduction in the load-bearing area or the initiation and subsequent propagation of fatigue cracks. This can be better illustrated by the Solomon parameter,[17,19] defined by

$$\Phi = 1 - F/F_M \quad (3)$$

where F is the maximum load at a certain load-cycle number, and F_M is the maximum load over the initial few cycles. An example showing the variation of the Solomon parameter with the fatigue cycles is shown in Fig. 13a, where $\Delta_T = \pm 10$ μm. Note that Φ

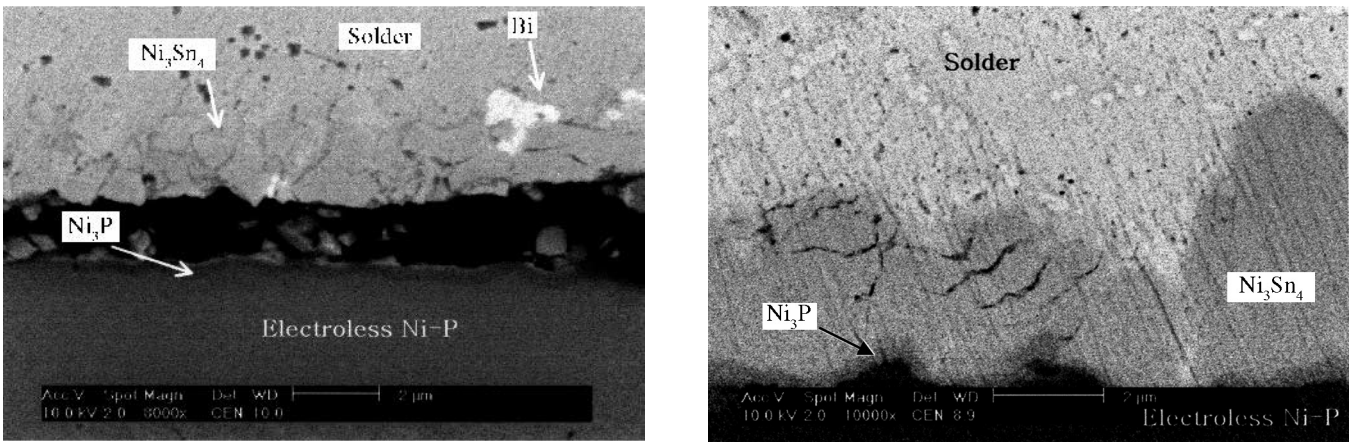

a b

Fig. 9. Backscattered SEM images of fatigue-fractured solder joints of (a) Sn-3.5Ag-7.5Bi and (b) Sn-3.5Ag alloys with the Au/Ni surface finish.

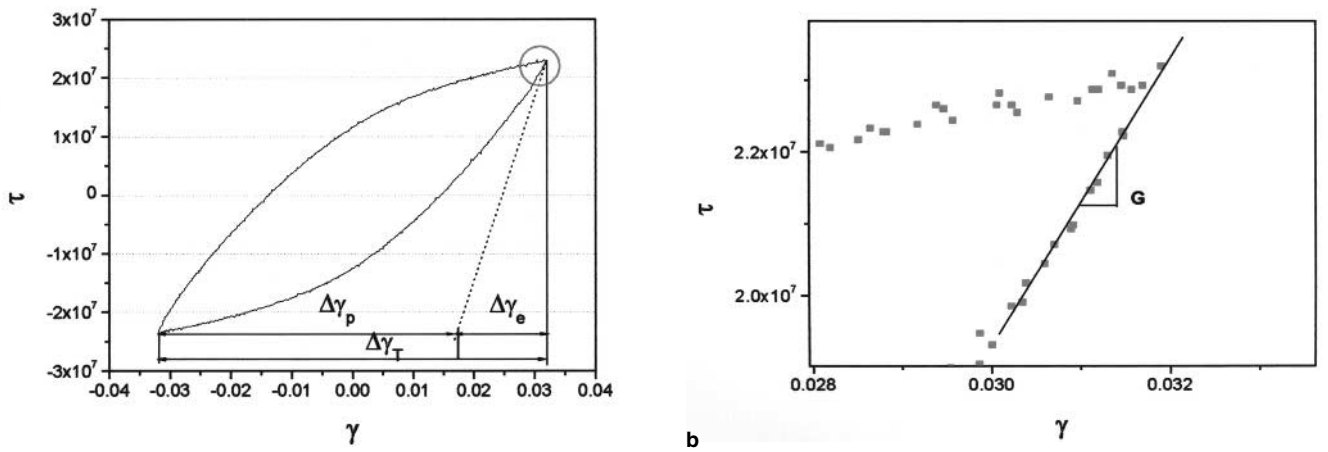

a b

Fig. 10. (a) Deduction of plastic strain ($\Delta\gamma_P$) from the load-strain hysteresis of the Sn-3.5Ag-0.75Cu alloy for $\Delta_T = \pm 20$ μm. (b) Detailed data points right after unloading and the derivation of shear modulus.

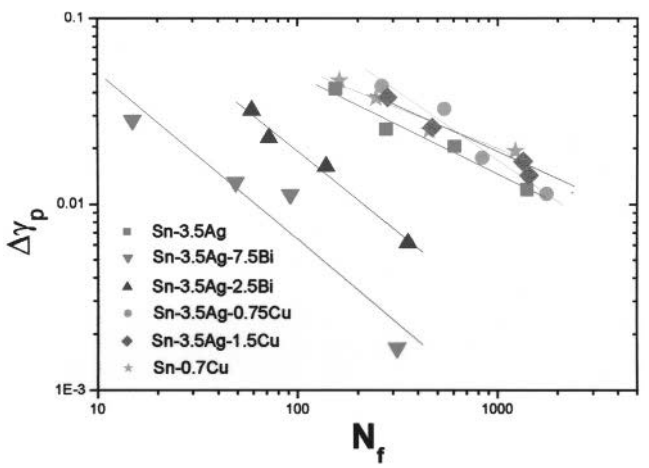

Fig. 11. Coffin–Manson's plot relating the fatigue life with the plastic strain range.

increased mildly during the initial stage but with a constant rate during the second stage, reflecting steady-state crack growth.[2] If a steady-state, load-drop rate, $(d\Phi/dN)_{SS}$, arbitrarily deduced from the Φ versus N_f plot, is correlated with the fatigue life cycle, as shown in Fig. 13b, the following relation can be deduced:

Table II. Material Constants of the Coffin–Manson Relation for Sn-Based Solder Alloys

Alloy	n	C
Sn-3.5Ag	0.57	0.83
Sn-3.5Ag-0.75Cu	0.74	2.87
Sn-3.5Ag-1.5Cu	0.53	0.74
Sn-3.5Ag-2.5Bi	0.87	1.05
Sn-3.5Ag-7.5Bi	0.90	0.41
Sn-0.7Cu	0.43	0.40

$$(d\Phi/dN)_{ss} \cdot N_f^{1.1} = C \quad (4)$$

Note that the load-drop rate increased in the order of Sn-3.5Ag-Cu, Sn-3.5Ag, Sn-0.7Cu, Sn-3.5Ag-2.5Bi, and Sn-3.5Ag-7.5Bi.

Up to now, the fatigue properties of Bi-containing Sn-3.5Ag alloys were significantly inferior to those of other alloys. One of the reasons for the poor performance of the Bi-containing alloys stems from the high stiffness of the solder matrix. Figure 14a shows variation of peak load in Fig. 6 with the total displacement, and the Bi-containing alloys showed higher peak loads than others because of the solid-solution hardening effect of Bi. The greater matrix

hardness of the Bi-containing alloys tends to increase the propensity for brittle cracking.[20] Similarly, $\Delta\gamma_p$ at peak loads using the method explained in Fig. 10 was plotted as a function of Δ_T in Fig. 14b, and the Bi-containing alloys had smaller $\Delta\gamma_p$ because of the high stiffness of the material. The trend of the peak load increase is the opposite of $\Delta\gamma_p$. The Sn-0.7Cu alloy had the lowest peak load and the largest $\Delta\gamma_p$, resulting in good fatigue properties. Therefore, a soft matrix and superior plastic flow capacity are important criteria to consider in the design of fatigue resistant materials.

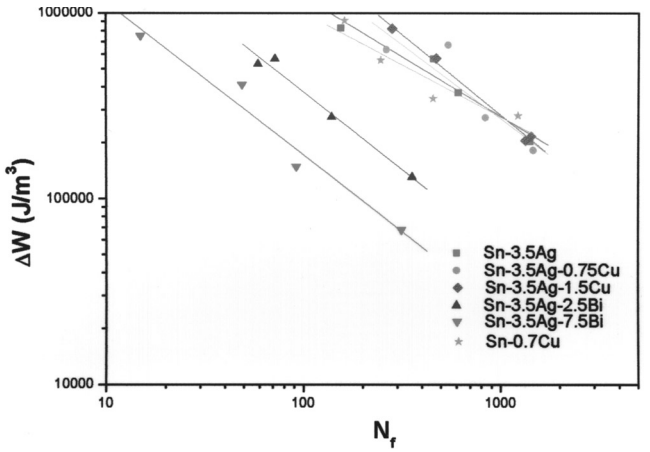

Fig. 12. Correlation between the plastic-strain energy density and the fatigue life (cycles).

CONCLUSIONS

- The fatigue properties of six Sn-based, Pb-free solders were investigated using lap-shear specimens with ball-grid-array solder balls on Au/Ni/Cu UBM. The Sn-3.5Ag, Sn-0.7Cu, and Sn-3.5Ag-Cu alloys had similar fatigue resistance, but fatigue resistance degraded with the addition of Bi.
- Cross-section SEM images showed the failure locus inside the solder matrix for the former group, but along the Ni_3P/Ni_3Sn_4 interface for the Bi-containing alloys. Interfacial cracking in the Bi-containing alloy was ascribed to Bi segregation to the interface, high residual stress in the region, and higher matrix hardness and stiffness of the Bi-containing alloys.
- The fatigue resistance analysis using the Coffin–Manson's relation, plastic-strain energy-based

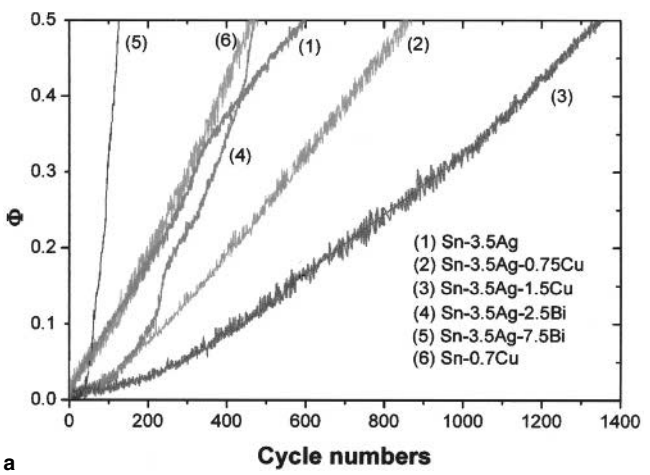

a

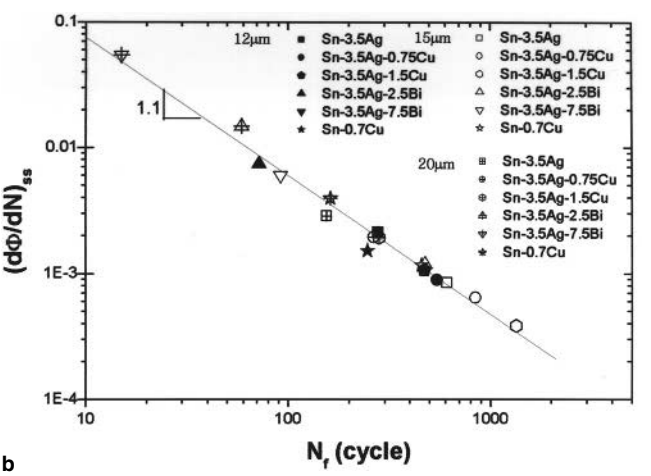

b

Fig. 13. (a) Solomon's load-drop parameter as a function of the fatigue cycle for various alloys. (b) Correlation between the steady-state load drop per cycle and the number of fatigue life (cycles).

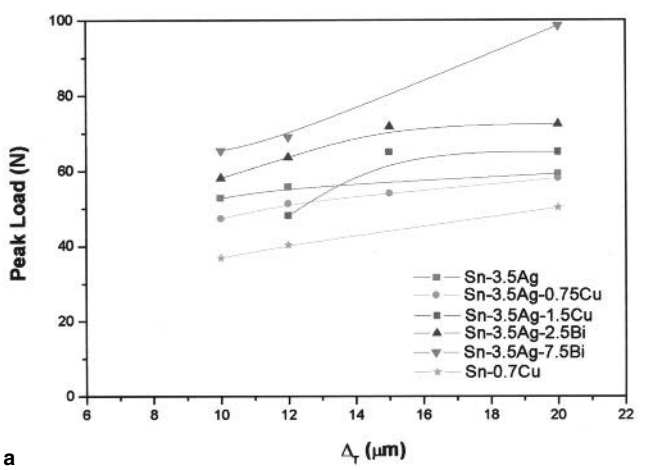

a

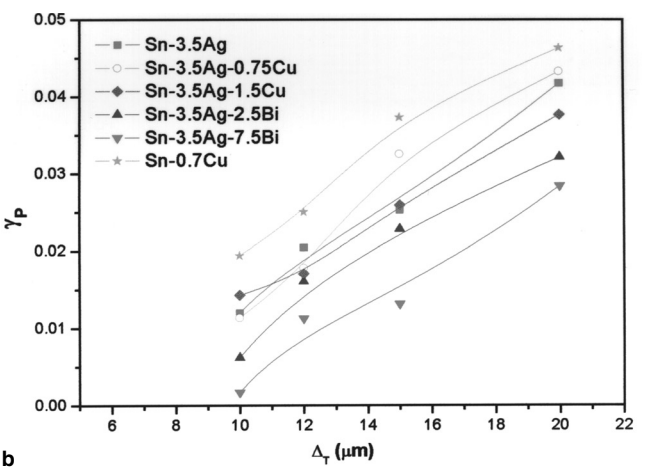

b

Fig. 14. (a) Peak loads of Pb-free solders. (b) Plastic strain range ($\Delta\gamma_P$) as function of the total displacement range (Δ_T).

Morrow model, and the Solomon parameter all gave consistent results.
- The Sn-0.7Cu eutectic alloy, which had poorer creep resistance than the Sn-3.5Ag-Cu alloys, had the same good fatigue resistance as Sn-3.5Ag and Sn-3.5Ag-Cu alloys because of the soft matrix and relatively higher compliance.

ACKNOWLEDGEMENTS

This work was supported by the Center for Electronic Packaging Materials, an engineering research center designated by the Korea Science and Engineering Foundation.

REFERENCES

1. H.J. Frost and M.F. Ashby, *Deformation-Mechanism Maps: the Plasticity and Creep of Metals and Ceramics* (New York: Pergamon Press, 1982), pp. 6–16.
2. Y. Kariya and M. Otsuka, *J. Electron. Mater.* 27, 1229 (1998).
3. C. Kanchanomai, Y. Miyahita, and Y. Mutoh, *Int. J. Fatigue* 24, 671 (2002).
4. J. Liang, N. Gollhardt, P.S. Lee, S.A. Schrodeder, and W.L. Morris, *Fatigue Fract. Eng., Mater. Struct.* 19, 1401 (1996).
5. C. Kanchanomai, S. Yamamoto, Y. Miyahsita, Y. Mutoh, and A.J. Mcevily, *Int. J. Fatigue* 24, 57 (2002).
6. S. Wen, L.M. Keer, and H. Mavoori, *J. Electron. Mater.* 30, 1190 (2001).
7. J. Zhao, Y. Mutoh, Y. Miyashita, and S.L. Mannan, *J. Electron. Mater.* 31, 879 (2002).
8. H.G. Song, J.W. Morris, Jr., and F. Hua, *JOM* 54, 30 (2002).
9. D.K. Joo, S.W. Shin, K.O. Lee, and J. Yu, *52nd Electronic Components Technology Conf.* (Piscataway, NJ: IEEE, 2002), pp. 1221–1225.
10. S.K. Kang, W.K. Choi, D.Y. Shin, P. Lauro, D.W. Henderson, T. Gosselin, and D.N. Leonard, *52nd Electronic Components Technology Conf.* (Piscataway, NJ: IEEE, 2002), pp. 146–153.
11. T.S. Park and S.B. Lee, *52nd Electronic Components Technology Conf.* (Piscataway, NJ: IEEE, 2002), pp. 979–984.
12. J.K. Lin, A.D. Silva, D. Frear, Y. Guo, J.W. Jang, L. Li, D. Mitchell, B. Yeung, and C. Zhang, *51st Electronic Components Technology Conf.* (Piscataway, NJ: IEEE, 2001), pp. 455–462.
13. E.A. Brandes, *Smithells Metals Reference Book* (London: Butterworths, 1983), pp. 11–211.
14. J.W. Jang, D.R. Frear, T.Y. Lee, and K.N. Tu, *J. Appl. Phys.* 88, 6359 (2000).
15. J.Y. Song and J. Yu, *Thin Solid Films* 415, 167 (2002).
16. S.W. Shin, K.O. Lee, and J. Yu (Paper presented at the 2003 TMS Annual Meeting, San Diego, CA, 2–6 March 2003).
17. H.D. Solomon and E.D. Tolksdorf: *J. Electron. Packaging* 118, 67 (1996).
18. X.Q. Shi, H.L.J. Pang, W. Zhou, and Z.P. Wang, *Scripta Mater.* 41, 289 (1999).
19. H.D. Solomon, *J. Electron. Packaging Trans. ASME* 113, 102 (1991).
20. S. Choi, K.N. Subramanian, J.P. Lucas, and T.R. Bieler, *J. Electron. Mater.* 29, 1249 (2000).